



# Super-hydrophilic MgO/NiCo<sub>2</sub>S<sub>4</sub> heterostructure for high-efficient oxygen evolution reaction in neutral electrolytes

Wei-Zhe Chen, Meng Zhang, Yang Liu, Xiao-Man Yao, Peng-Yu Liu, Zhiliang Liu, Jinlu He\*, Yan-Qin Wang\*

Inner Mongolia Key Laboratory of Chemistry and Physics of Rare Earth Materials, College of Chemistry and Chemical Engineering, Inner Mongolia University, Huhhot 010021, China

## ARTICLE INFO

### Keywords:

Heterostructure  
Oxygen evolution reaction  
pH-neutral electrolyte  
Hydration-effect-promoting element  
Electronic structure adjustment

## ABSTRACT

Oxygen evolution reaction (OER) in pH-neutral electrolyte is considered more difficult for the additional adsorption and the dissociation process of H<sub>2</sub>O. Herein, by in-suit construction of the heterostructure between MgO and NiCo<sub>2</sub>S<sub>4</sub> on carbon cloth (CC), a novel MgO/NiCo<sub>2</sub>S<sub>4</sub> heterostructure on CC (MgO/NCS-CC) is successfully fabricated. Benefitting from the optimized electronic structure attributed to the construction of hetero-interface, and the intense adsorption of H<sub>2</sub>O on the surface of catalysts owing to the introduction of hydration-effect-promoting (HEP) element Mg, the MgO/NCS-CC exhibits outstanding OER activity with overpotential of 145 mV at the current density of 10 mA·cm<sup>-2</sup> in pH-neutral electrolyte and can maintain stability over 40 h. Density-functional theory (DFT) also demonstrates that the MgO/NiCo<sub>2</sub>S<sub>4</sub> heterostructure can effectively adjust the electronic structure and enhance the adsorption of reactant, thus further optimizing Gibbs free energies and improving the activity for OER in pH-neutral electrolyte.

## 1. Introduction

The oxygen evolution reaction (OER) plays a pivotal role in the field of energy storage and conversion, such as metal-air batteries, fuel cells, water splitting into hydrogen [1], CO<sub>2</sub> reduction and NH<sub>3</sub> production [2]. Compared with OER in alkaline electrolyte, OER in pH-neutral electrolyte has the advantages of environmentally friendly, almost no corrosion and can reduce the cost of electrolytic cell [3–5]. Additionally, the key to microbial electrolysis of cells is the pH-neutral electrolyte, which does not harm microbial growth [6]. More importantly, for electrochemical CO<sub>2</sub> reduction, the pH-neutral electrolyte can facilitate the dissolution of more CO<sub>2</sub> molecules and restrain the competing hydrogen evolution reaction, therefore, the efficiency of electrochemical CO<sub>2</sub> reduction is mainly limited by OER process [7]. However, in pH-neutral electrolyte, the extremely sluggish OER which is caused by the low concentration of reactants absorbed on the surface limits the efficiency of many applications, even high-efficient and costly noble metal catalysts are used for neutral water oxidation [8]. Transitional metal chalcogenides (TMCs) which possess an open framework, unique electrochemical properties and relative economic price have been regarded as the substitution for noble metal catalysts [9,10]. However,

the insufficient active sites, inferior durability and the low conductivity greatly limit the activity of TMCs for OER [11]. Therefore, it is imperative and urgent to develop a high-efficiency and economic OER catalysts in pH-neutral electrolyte.

Generally speaking, there are four steps of OER under pH-neutral condition [12]:



It can be obviously seen that the adsorption and the dissociation processes of H<sub>2</sub>O are necessary for OER in pH-neutral condition, compared with those in alkaline condition [13], which is one of the important reasons that OER in pH-neutral condition is more difficult than that in alkaline. Hence, enhancing the adsorption of reactants on the catalyst surface and adjusting the electronic structure of catalysts are the valid methods to improve the activity of catalysts for neutral water oxidation [14,15]. As one type of hydration-effect-promoting (HEP)

\* Corresponding authors.

E-mail addresses: [hejinlu@imu.edu.cn](mailto:hejinlu@imu.edu.cn) (J. He), [yqwang\\_chem@imu.edu.cn](mailto:yqwang_chem@imu.edu.cn) (Y.-Q. Wang).

<https://doi.org/10.1016/j.apcatb.2022.121432>

Received 28 December 2021; Received in revised form 11 March 2022; Accepted 17 April 2022

Available online 20 April 2022

0926-3373/© 2022 Elsevier B.V. All rights reserved.

metal,  $\text{Mg}^{2+}$  demonstrates a high hydration energy which can improve the adsorption of  $\text{H}_2\text{O}$  on the catalyst surface. Previous work has reported that the introduction of  $\text{Mg}^{2+}$  into Ni-Fe catalyst system enhanced water adsorption and improved the OER activity in pH-neutral electrolyte [16]. Therefore, it is feasible to improve the catalytic efficiency by introducing HEP Mg element to promote the adsorption of water molecules on the catalyst surface for neutral water oxidation.

Additionally, it is reported that the construction of the heterostructure can redistribute the electron and further regulate the electronic structure and surface binding energy of the catalysts, which is highly effective to improve the activity of catalysts [17]. Besides, heterostructure is favorable for promoting the activity of the catalyst in multistep reactions, like in OER reactions [18]. Recently, Wang et al. reported a highly efficient OER catalyst  $\text{NiCo}_2\text{S}_4/\text{ZnS}$ , which was a  $\text{NiCo}_2\text{S}_4/\text{ZnS}$  heterojunction containing ZnS nanoparticles with Zn defect anchored onto the  $\text{NiCo}_2\text{S}_4$  surface, and showed excellent OER performance with an ultralow overpotential of 140 mV at the current density of  $10 \text{ mA} \cdot \text{cm}^{-2}$  in 1 M KOH. This  $\text{NiCo}_2\text{S}_4/\text{ZnS}$  catalyst system is a representative of heterostructure catalyst used for improving the OER activity, however, it is noted that the OER catalytic system is alkaline, not pH-neutral [11].

Inspired by the above research,  $\text{MgO}/\text{NiCo}_2\text{S}_4$  heterostructure on carbon cloth ( $\text{MgO}/\text{NCS-CC}$ ) was successfully synthesized herein. Benefiting from the high hydration energy of HEP element Mg, the surface adsorption of  $\text{H}_2\text{O}$  for  $\text{MgO}/\text{NCS-CC}$  was significantly enhanced. Moreover, the formation of the heterostructure between MgO and  $\text{NiCo}_2\text{S}_4$  can regulate the electronic structure of the catalyst to the states which are more suitable for OER in pH-neutral condition. Thus, the self-supported electrode on carbon cloth enhanced the electrocatalyst/electrolyte contact and accelerated the charge transfer [19,20], providing abundant active sites and facilitating the bubble detachment [21,22]. Surprisingly, the as-prepared  $\text{MgO}/\text{NCS-CC}$  exhibits outstanding OER activity in pH-neutral electrolyte with an ultralow overpotential of 145 mV at the current density of  $10 \text{ mA} \cdot \text{cm}^{-2}$ , which the overpotential is the lowest among all kinds of OER catalysts in neutral water oxidation reactions reported. Furthermore,  $\text{MgO}/\text{NCS-CC}$  possesses excellent stability, which can remain stable over 40 h. Density functional theory (DFT) calculation also reveals that the construction of heterostructure between MgO and  $\text{NiCo}_2\text{S}_4$  can modify the electronic structure effectively, and increase the adsorption of  $\text{H}_2\text{O}$  on surface of catalyst and further decrease the Gibbs free energies of rate-determining step (RDS), which is the pivotal reason that the OER activity can be improved for  $\text{MgO}/\text{NCS-CC}$  in neutral water oxidation. This research provides a new strategy to prepare a highly efficient non-noble metal OER catalyst containing heterostructure and HEP element in pH-neutral condition, and affords implications for electrocatalytic research.

## 2. Experimental section

### 2.1. Synthesis of $\text{MgO-CC}$

1.2 g  $\text{Mg}(\text{NO}_3)_2 \cdot 6 \text{H}_2\text{O}$  was first dissolved in 20 mL deionized water. After that, a small piece of clean carbon cloth (CC) ( $1 \text{ cm} \times 1 \text{ cm}$ ) was put inside the clamping piece electrode and immersed into the solution of  $\text{Mg}(\text{NO}_3)_2 \cdot 6 \text{H}_2\text{O}$ . Three-electrode system was used to electrodeposit  $\text{Mg}^{2+}$  on CC at the voltage of  $-1 \text{ V}$  verse RHE for 100 s of each side. After drying for over 6 h in vacuum oven, the CC with  $\text{Mg}^{2+}$  was annealed in muffle furnace at  $350^\circ\text{C}$  in air atmosphere for 1 h. The obtained product was named  $\text{MgO-CC}$ .

### 2.2. Synthesis of $\text{MgO}/\text{NCO-CC}$

0.43 g  $\text{Co}(\text{NO}_3)_2 \cdot 6 \text{H}_2\text{O}$ , 0.43 g  $\text{Ni}(\text{NO}_3)_2 \cdot 6 \text{H}_2\text{O}$  and 0.9 g urea were dissolved in 10 mL deionized water. Then the as-prepared solution and  $\text{MgO-CC}$  were transferred into a Teflon-lined autoclave and kept at  $120^\circ\text{C}$  for 12 h. The obtained product and CC were washed several times

and dried in vacuum oven for 6 h. Finally, the as-prepared precursor was annealed in muffle furnace at  $450^\circ\text{C}$  in air atmosphere for 2 h. The product  $\text{NiCo}_2\text{O}_4\text{-CC}$  was named  $\text{MgO}/\text{NCO-CC}$ .

### 2.3. Synthesis of $\text{MgO}/\text{NCS-CC}$

0.05 g the as-prepared  $\text{NiCo}_2\text{O}_4$  powder and 0.15 g thioacetamide (TAA) were dissolved in 10 mL deionized water. Then, the solution and  $\text{MgO}/\text{NCO-CC}$  were together transferred into a Teflon-lined autoclave and kept at  $160^\circ\text{C}$  for 12 h. After washing with water, the finally obtained product was named  $\text{MgO}/\text{NCS-CC}$ .

### 2.4. Synthesis of $\text{NCS-CC}$

Compared with the synthetic method of  $\text{MgO}/\text{NCS-CC}$ , the only difference of the synthesis of  $\text{NCS-CC}$  is that the addition of  $\text{MgO}$  is not involved.

### 2.5. Synthesis of $\text{RuO}_2\text{-CC}$

10  $\mu\text{L}$  Nafion (5 wt%) and 4 mg  $\text{RuO}_2$  were dispersed in 400  $\mu\text{L}$  of anhydrous ethanol by sonication for 60 mins. Then 200  $\mu\text{L}$  solution was dropped on carbon cloth (CC) and dried at  $60^\circ\text{C}$  for 12 h.

### 2.6. Materials characterization

XRD was measured by a PANalytical Empyrean diffractometer at a scanning rate of  $0.013^\circ$  in the Bragg angle ranging between  $5^\circ$  and  $80^\circ$  with Cu  $K\alpha$  radiation ( $\lambda = 1.5418 \text{ \AA}$ ). Scanning electron micrographs were measured by a HITACHI SU5000 + scanning electron microscope (SEM). Transmission electron microscopy and energy-dispersive X-ray (EDX) spectrum characterizations were performed on an FEI F20 transmission electron microscope (TEM). X-ray photoelectron spectroscopy (XPS) measurements were performed by a Thermo Fisher K-Alpha which was equipped with two ultrahigh vacuum (UHV) chambers. And all spectra were calibrated with the C-C peak of C 1 s orbitals as 284.8 eV. Contact angle (CA) was measured by Dataphysics OCA20. Fourier transform infrared (FTIR) spectroscopy (KBr disk) was recorded in the range of  $500\text{--}4000 \text{ cm}^{-1}$  using KBr pellets on a TENSOR 27 FI-IR spectrophotometer.

### 2.7. Electrochemical measurements

All electrochemical measurements were carried out on a CHI660E electrochemical workstation by three-electrode electrochemical system in  $\text{CO}_2$ -saturated 0.5 M  $\text{KHCO}_3$  solution at room temperature. Carbon rod used as the counter electrodes. The reference electrode was  $\text{Ag}/\text{AgCl}$  electrode, and the working electrode was  $1 \times 1 \text{ cm}^2$  electrocatalyst. Linear sweep voltammetry (LSV) polarization curves in the voltage range of  $1\text{--}2 \text{ V}$  verse RHE for OER, and proceeded in  $\text{CO}_2$ -saturated 0.5 M  $\text{KHCO}_3$  solution at a scan rate of  $2 \text{ mV} \cdot \text{s}^{-1}$ . The amperometric current density-time ( $i\text{--}t$ ) was also measured in  $\text{CO}_2$ -saturated 0.5 M  $\text{KHCO}_3$  solution. The accelerated durability tests (ADTs) were proceeded for 2000 CV cycles in  $\text{CO}_2$ -saturated 0.5 M  $\text{KHCO}_3$  and in the voltage range of  $1\text{--}2 \text{ V}$  verse RHE. Electrochemical impedance spectroscopy (EIS) was performed at overpotential of 200 mV, and in the frequency range from 10 kHz to 0.04 Hz. The electrochemical surface areas (ECSAs) were obtained by the double-layer capacitance ( $C_{dl}$ ). The electroactive surface areas were measured in the voltage of  $0.723\text{--}0.823 \text{ V}$  verse RHE by cyclic voltammetry (CV) with various scan rates ranging from  $20 \text{ mV} \cdot \text{s}^{-1}$  to  $100 \text{ mV} \cdot \text{s}^{-1}$ .

### 3. Results and discussion

#### 3.1. Materials synthesis and structure

##### 3.1.1. Synthesis of MgO/NCS-CC

As shown in Fig. 1a, the MgO/NCS-CC heterostructure was fabricated by multi-step reactions. Firstly, MgO was grown in-situ on carbon cloth (CC) by electrodeposition and subsequent annealing in air. Then, by utilizing the methods of hydrothermal synthesis and annealing,  $\text{NiCo}_2\text{O}_4$  was successfully in-situ formed on MgO-CC. Finally, the MgO/NCS-CC heterostructure was obtained through sulphuration step. For comparison, the  $\text{NiCo}_2\text{S}_4$ -CC (NCS-CC) sample which does not contain the heterostructure formed with MgO was also synthesized by above method. Moreover, the corresponding morphological representation of the sample obtained at each step is also given.

X-ray diffraction (XRD) patterns were used to identify the structure of MgO/NCS-CC and other reference samples (Fig. S1, Supplementary

data). The diffraction peaks of MgO-CC sample can be easily matched to MgO (JCPDF No.45-0946), and the characteristic diffraction peaks located at  $36.9^\circ$ ,  $42.9^\circ$ ,  $62.3^\circ$ , and  $78.6^\circ$  are respectively attributed to the (111), (200), (220), and (222) facets of MgO (Fig. S1a, Supplementary data). Moreover, the XRD patterns of MgO/ $\text{NiCo}_2\text{O}_4$  on CC (MgO/NCO-CC) and MgO/ $\text{NiCo}_2\text{S}_4$  on CC (MgO/NCS-CC) also contain several diffraction peaks consistent with those of MgO, only with decreased intensity, which indicates that both MgO/NCO-CC and MgO/NCS-CC contain MgO phase, while the decreased intensity could be induced by the only surface growth of  $\text{NiCo}_2\text{S}_4$  and  $\text{NiCo}_2\text{O}_4$  on MgO. Additionally, the diffraction peaks of MgO/NCO-CC also show the peaks at  $31.1^\circ$ ,  $36.7^\circ$ ,  $44.6^\circ$ ,  $59.1^\circ$  and  $64.9^\circ$ , which can be respectively attributed to (220), (311), (400), (511) and (440) facets of  $\text{NiCo}_2\text{O}_4$  (JCPDF No.20-0781), suggesting the precursor  $\text{NiCo}_2\text{O}_4$  is contained in MgO/NCO-CC. After the sulphuration by hydrothermal treatment, the XRD diffraction peaks of MgO/NCS-CC at  $16.3^\circ$ ,  $31.6^\circ$ ,  $33.0^\circ$ ,  $38.3^\circ$ ,  $50.5^\circ$ , and  $55.3^\circ$  can be respectively ascribed to (111), (311), (222),

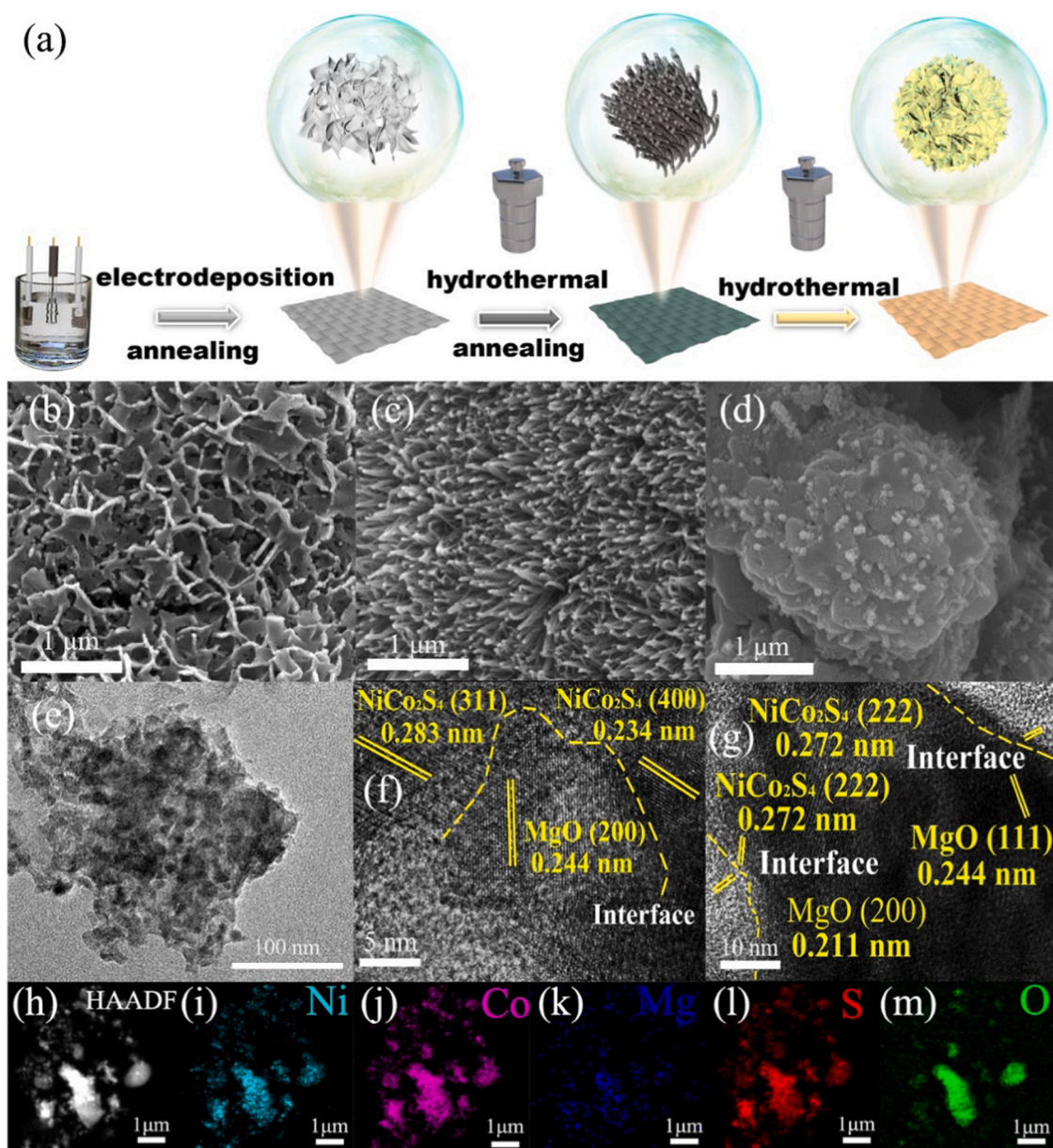


**Fig. 1.** (a) Schematic illustration of the synthetic strategy and the morphology regulation for the MgO/NCS-CC heterostructure. (b-d) SEM images of MgO-CC, MgO/NCO-CC and MgO/NCS-CC, respectively. (e) TEM images of MgO/NCS-CC. (f-g) HRTEM images of MgO/NCS-CC. (h-m) HAADF-STEM and elemental mapping of MgO/NCS-CC.

(400), (511) and (440) facets of  $\text{NiCo}_2\text{S}_4$  (JCPDF No.20-0781), demonstrating the successful synthesis of  $\text{NiCo}_2\text{S}_4$ , which is contained in  $\text{MgO}/\text{NCS-CC}$ . Meanwhile, the XRD peaks of  $\text{NCS-CC}$  ( $\text{NiCo}_2\text{S}_4$  on CC) sample also matches well with those of  $\text{NiCo}_2\text{S}_4$  (JCPDF No.20-0781), which suggests the successful synthesis of the contrast sample in comparison with  $\text{MgO}/\text{NCS-CC}$ , without containing  $\text{MgO}$  (Fig. S1b, Supplementary data).

### 3.1.2. Structure and morphology regulation

The scanning electron microscopy (SEM) was used to characterize the morphologies and structures of  $\text{MgO}/\text{NCS-CC}$  and other reference samples. The SEM image of  $\text{MgO-CC}$  indicates that it is composed of randomly distributed nanosheets (Fig. 1b). For  $\text{MgO}/\text{NCO-CC}$ , it shows regular nanorod array (Fig. 1c), while after the sulphuration by hydrothermal, the morphology of  $\text{MgO}/\text{NCS-CC}$  changed into the nanoflower-like morphology. Furthermore, from the SEM images, it can also be clearly seen that there are lots of tiny particles dispersed on the nanoflower (Fig. 1d). Meanwhile, the SEM images of  $\text{MgO-CC}$ ,  $\text{MgO}/\text{NCO-CC}$  and  $\text{MgO}/\text{NCS-CC}$  in a larger magnification demonstrate that  $\text{MgO}$ ,  $\text{NiCo}_2\text{O}_4$  and  $\text{NiCo}_2\text{S}_4$  have grown evenly on CC (Fig. S2, Supplementary data). In addition, as depicted in Fig. S3a (Supplementary data),  $\text{NCS-CC}$  shows a uniform dispersion on CC and an urchin-like morphology which

is obviously different from that of  $\text{MgO}/\text{NCS-CC}$ , which the morphology difference indicates that the construction of the heterostructure between  $\text{MgO}$  and  $\text{NiCo}_2\text{S}_4$  can significantly change the morphology of  $\text{NiCo}_2\text{S}_4$ . To get the further information of the morphology and structure of  $\text{MgO}/\text{NCS-CC}$ , transmission electron microscopy (TEM) test was also carried out, which also exhibits the morphology of nanoflower with tiny particles on it, and is consistent with the SEM result (Fig. 1e). Moreover, the high-resolution TEM (HR-TEM) was used to survey the lattice fringe of  $\text{MgO}/\text{NCS-CC}$ . The fringe spacing 0.234 nm and 0.283 nm can be respectively attributed to (400) and (311) crystal facets of  $\text{NiCo}_2\text{S}_4$ , and the fringe spacing 0.244 nm matches well with (111) facet of  $\text{MgO}$ . Notably, an obvious interface between  $\text{MgO}$  and  $\text{NiCo}_2\text{S}_4$  can be observed, which confirms the successful construction of the heterostructure  $\text{MgO}/\text{NCS-CC}$  (Fig. 1f) [23]. In addition, the fringe spacing 0.272 nm ascribed to (222) facet of  $\text{NiCo}_2\text{S}_4$ , and the fringe spacing of 0.272 nm attributed to (200) facet of  $\text{MgO}$  can also be observed (Fig. 1g), which demonstrates diverse crystal planes and interfaces were exposed in  $\text{MgO}/\text{NCS-CC}$  (Fig. 1g). Moreover, the exposed fringe spacing from HR-TEM is also consistent with the XRD result. Furthermore, the energy dispersive X-ray spectroscopy (EDX) mapping exhibits the uniform distribution of Ni, Co, Mg, S and O elements in  $\text{MgO}/\text{NCS-CC}$  (Fig. 1h-m). Additionally, as shown in Fig. S4 (Supplementary data),

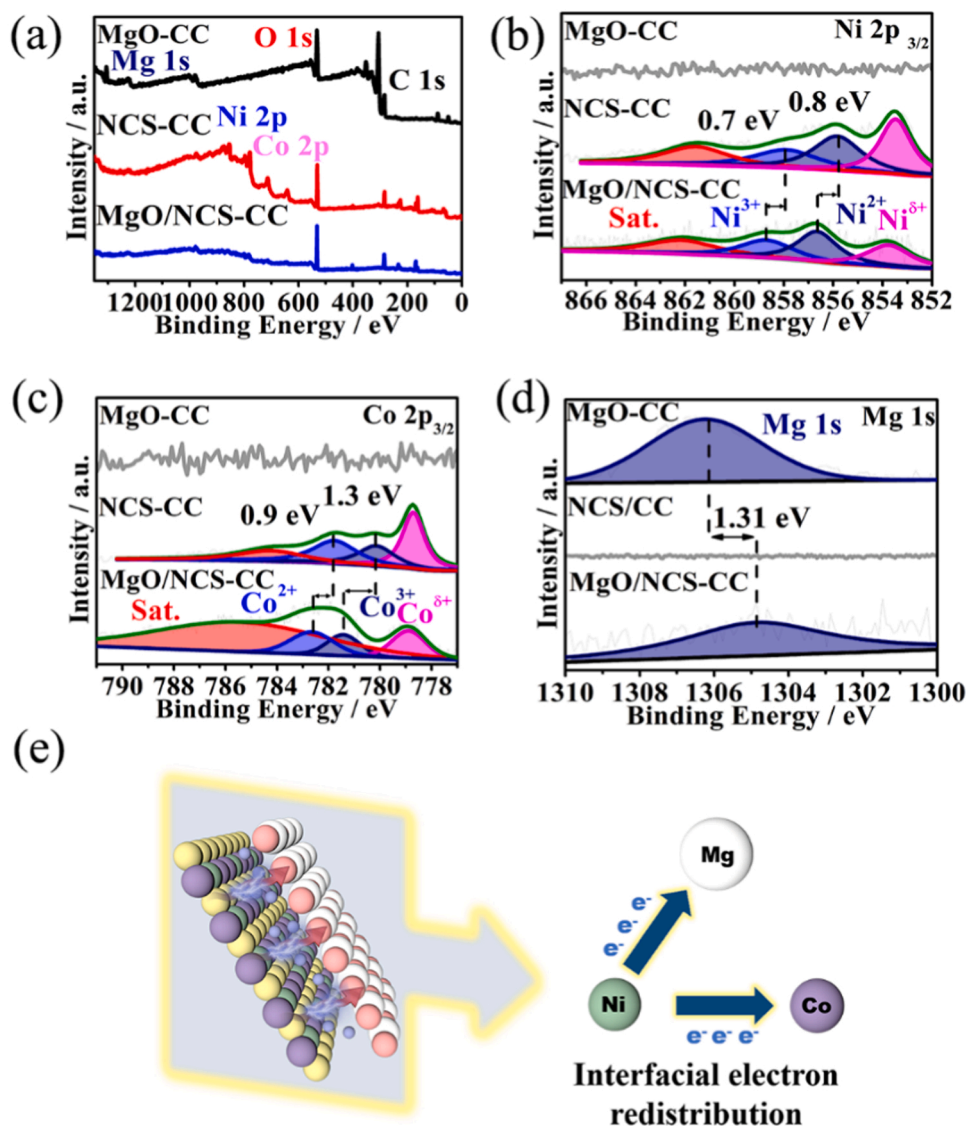


**Fig. 2.** (a) Survey XPS spectra of  $\text{MgO-CC}$ ,  $\text{MgO}/\text{NCO-CC}$  and  $\text{MgO}/\text{NCS-CC}$ . (b-d) The high-resolution XPS spectra of  $\text{MgO-CC}$ ,  $\text{NCS-CC}$  and  $\text{MgO}/\text{NCS-CC}$ : Ni  $2p_{3/2}$ , Co  $2p_{3/2}$  and Mg  $1s$ , respectively. (e) Schematic illustration of the electron transfer path in  $\text{MgO}/\text{NiCo}_2\text{S}_4$ .

The contents of Mg, Ni, Co, S and O are also estimated by the results of EDS mapping, which the atomic percentage contents of Mg, Ni, Co, S and O are 1.88%, 2.73%, 3.66%, 20.63% and 71.10%, respectively.

### 3.1.3. Surface chemical composition and valence states

In order to survey the near-surface composition and the electronic structure of MgO/NCS-CC and its reference samples, X-ray photoelectron spectroscopy (XPS) was applied. The survey XPS spectra of MgO/NCS-CC clearly reveals the existence of Ni, Co, Mg, S and O elements [24,25]. Besides, the absence of Ni and Co peaks in MgO-CC spectra and Mg in NCS-CC spectra indicates that the heterostructure is not contained in MgO-CC and NCS-CC samples (Fig. 2a). The high-resolution XPS spectra of Ni  $2p_{3/2}$  of NCS-CC reveals the peaks located at 861.6 eV, 853.5 eV, 855.8 eV and 857.9 eV are respectively ascribed to the satellite peak,  $Ni^{6+}$  species,  $Ni^{2+}$  and  $Ni^{3+}$  in NCS-CC [21]. The existence of  $Ni^{2+}$  and  $Ni^{3+}$  can act as the redox transformation couple, which can promote the electron transport, thereby being advantageous to the highly efficient electrocatalytic reactions [26]. However, after the construction of heterostructure between MgO and  $NiCo_2S_4$ , the binding energy of both  $Ni^{2+}$  and  $Ni^{3+}$  in MgO/NCS-CC up-shifts of 0.8 eV and 0.7 eV compared with those of NCS-CC. The positive shifts of  $Ni^{2+}$  and  $Ni^{3+}$  peaks in MgO/NCS-CC indicate that the electron density around Ni species decreases after the formation of the heterostructure, which is beneficial for boosting the activity of catalysts (Fig. 2b) [26–29]. For Co  $2p_{3/2}$  in Fig. 2c, the peaks at 784.2 eV, 778.7 eV, 780.1 eV and 781.8 eV represent the satellite peak,  $Co^{6+}$  species,  $Co^{3+}$  and  $Co^{2+}$  in NCS-CC, respectively [21,30]. The binding energy of  $Co^{3+}$  and  $Co^{2+}$  also up-shifts of 1.3 eV and 0.9 eV, respectively. However, being different from the analysis of Ni, this positive shift of the binding energy of Co means the increase of electron density around Co species after the formation of the heterostructure (Fig. 2c) [7,31]. Moreover, the XPS spectra shows no any peaks of Ni  $2p_{3/2}$  and Co  $2p_{3/2}$  in MgO-CC, which means the absence of Ni and Co elements. In addition, the peak of MgO at 1306.1 eV is assigned to Mg 1s [32]. However, being opposite to the situations of Ni and Co elements, the peak of Mg s in MgO/NCS-CC down-shifts of 1.31 eV compared with that of NCS-CC, which indicates the electron density around Mg increases (Fig. 2d) [24,33].

Furthermore, the high-resolution XPS spectra of S and O are also given in Fig. S4. For MgO/NCS-CC, the peaks at 532.93 eV and 531.99 eV are respectively assigned to C-O and Mg-O bonds in Fig. S4a (Supplementary data) [15,34], and the peaks at 163.4, 162.60 and 161.64 eV are attributed to M-S bond, S  $2p_{3/2}$  and S  $2p_{1/2}$ , respectively (Fig. S5b, Supplementary data) [11]. Notably, the peaks of Mg-O bond up-shifts of 0.42 eV while the S  $2p_{3/2}$  and S  $2p_{1/2}$  respectively down-shift of 0.42 and 0.16 eV in MgO/NCS-CC, compared with NCS-CC. The shifts of the binding energy of O and S in MgO/NCS-CC demonstrate that strong electronic interactions exist between MgO and  $NiCo_2S_4$  after the formation of heterostructure. The adjustment of the electronic structure of MgO/NCS-CC may further enhance the OER performance [11,35,36]. Thus, the above XPS results indicate the successful construction of the heterostructure between MgO and  $NiCo_2S_4$  and confirm that the construction of the heterostructure can effectively regulate the electronic structure of MgO/NCS-CC, and the electrons flow from Ni to Co and Mg [37]. Specifically, the construction of heterostructure can lead to the charge redistribution and further the change of the local electron configuration at the interface between MgO and  $NiCo_2S_4$ , which may boost the electrocatalytic activity of the catalyst (Fig. 2e) [38].

### 3.1.4. Adsorption of $H_2O$ of MgO/NCS-CC

In order to further confirm the adsorption of reactants on NCS-CC and MgO/NCS-CC, the contact angles (CA) were also tested. The contact angle between NCS-CC and  $H_2O$  is 33.4° and indicates that  $NiCo_2S_4$  has good hydrophilicity (Fig. 3a). However, after the introduction of hydration-effect-promoting (HEP) metal Mg by the method of constructing heterostructure between MgO and  $NiCo_2S_4$ , the contact angle of MgO/NCS-CC remarkably decreased to 0°, which is the super-hydrophilicity state and suggests the strong adsorption ability of MgO/NCS-CC to  $H_2O$  molecules (Fig. 3b). The dynamic change of the contact angle of MgO/NCS-CC with time is shown in Fig. S6 (Supplementary data) and (Supporting Video S1). As is known that the enhancement of water adsorption is of great importance for increasing the efficiency of neutral water oxidation. The CA test demonstrates the successful application of the strategy of enhancing  $H_2O$  adsorption by introducing the HEP Mg element in the catalyst. As reported by Sargent

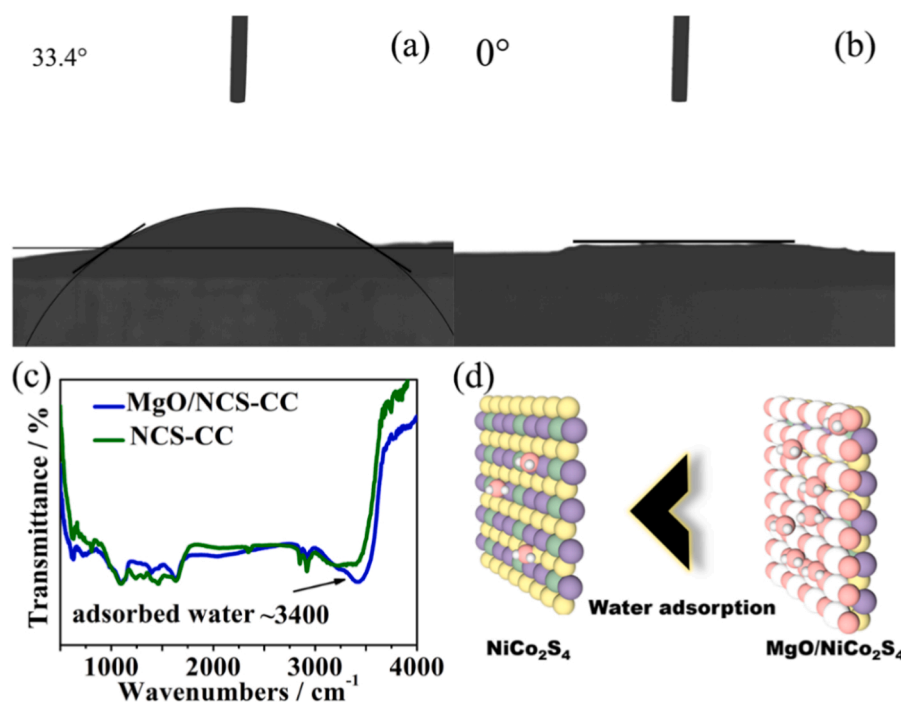


**Fig. 3.** (a–b) The contact angle measurement results of NCS-CC (a) and MgO/NCS-CC (b), respectively. (c) FTIR spectra of NCS-CC and MgO/NCS-CC. (d) Schematic illustration of the water adsorption comparison between  $NiCo_2S_4$  and MgO/ $NiCo_2S_4$ .

et al. that  $\text{Mg}^{2+}$  ions can enhance the bond strength between the catalyst surface and molecular water thereby improving the adsorption of water molecules on the catalyst [16]. The  $\text{Mg}^{2+}$  in  $\text{MgO}/\text{NCS-CC}$  also can effectively contact with  $\text{H}_2\text{O}$  and enhance the bond strength between the catalyst surface and water molecule and enhance the adsorption of water on the surface of electrocatalyst. In addition, to further verify the enhancement of water adsorption by  $\text{MgO}/\text{NCS-CC}$ , Fourier transform infrared (FTIR) spectroscopy was also used to compare with that of  $\text{NCS-CC}$ . As shown in Fig. 3c, the peak intensity at  $\approx 3400\text{ cm}^{-1}$  reveals the amount of adsorbed water, which the amount of adsorbed water of  $\text{MgO}/\text{NCS-CC}$  is obviously greater than that absorbed by  $\text{NCS-CC}$ , confirming that the heterostructure  $\text{MgO}/\text{NCS-CC}$  effectively enhanced the water adsorption [16], which should be advantageous to boost the OER activity in pH-neutral electrolyte.

doi:10.1016/j.apcatb.2022.121432

### 3.2. Electrocatalytic performance

The OER activity of  $\text{MgO}/\text{NCS-CC}$  and other reference samples were tested by three-electrode configuration in  $\text{CO}_2$ -saturated 0.5 M  $\text{KHCO}_3$  ( $\text{pH} \approx 8.5$ ) with 95% iR correction. The liner sweep voltammetry (LSV) curves show that the overpotential of  $\text{MgO}/\text{NCS-CC}$  (145 mV) at  $10\text{ mA}\cdot\text{cm}^{-2}$  is much lower than that of  $\text{NCS-CC}$  (233 mV) and  $\text{RuO}_2\text{-CC}$  (441 mV), while  $\text{MgO-CC}$ ,  $\text{MgO}/\text{NCO-CC}$  and  $\text{CC}$  have no OER activity (Fig. 4a). The lower overpotential of  $\text{MgO}/\text{NCS-CC}$  is a convincing evidence which indicates that the construction of the heterostructure between  $\text{MgO}$  and  $\text{NiCo}_2\text{S}_4$  can effectively improve the OER activity, which can be further attributed to the optimization of the electronic structure and the enhancement of the adsorption of  $\text{H}_2\text{O}$ . In addition, it is noted that the overpotentials of  $\text{MgO}/\text{NCS-CC}$  and  $\text{NCS-CC}$  are 310 mV and 390 mV at the larger current density of  $100\text{ mA}\cdot\text{cm}^{-2}$ , respectively, while other control samples even can't reach the current density of  $100\text{ mA}\cdot\text{cm}^{-2}$  in the tested potential range during the OER test, suggesting excellent OER performance of  $\text{MgO}/\text{NCS-CC}$  for potential application. Furthermore, to explore the influence of Mg content on the structure and OER performance of the catalyst, two samples of  $\text{Mg}^{2+}$  ions electrodeposited on carbon cloth for different electrodeposition time (100 s and 200 s) have also been synthesized. The samples are

respectively named as  $\text{MgO}/\text{NCS-CC}$  (100 s) and  $\text{MgO}/\text{NCS-CC}$  (200 s), which the sample with the longer electrodeposition time implies a higher  $\text{Mg}^{2+}$  ions content on the carbon cloth. The obtained two samples were further treated with the same subsequent procedure. As displayed in Fig. S7a in the Supplementary data, the XRD comparison between  $\text{MgO}/\text{NCS-CC}$  (100 s) and  $\text{MgO}/\text{NCS-CC}$  (200 s) indicates that there is almost no structure change. Moreover, the LSV cures of  $\text{MgO}/\text{NCS-CC}$  (100 s) and  $\text{MgO}/\text{NCS-CC}$  (200 s) in Fig. S7b (Supplementary data) also exhibit that there is only a negligible change of OER performance between them, suggesting the content of Mg of the catalyst has almost no effect on the structure and the electrocatalytic OER performance.

Moreover, the turnover frequency (TOF) values of  $\text{MgO}/\text{NCS-CC}$  and  $\text{NCS-CC}$  are also calculated by the crystallographic parameters of  $\text{MgO}$  and  $\text{NiCo}_2\text{S}_4$  (Fig. S8, Supplementary data), and the detailed calculation is shown in the Supporting Information. Obviously, the TOF value of  $\text{MgO}/\text{NCS-CC}$  is higher than that of  $\text{NCS-CC}$  within the tested potential range of OER, which indicates that each electrocatalytic active site of  $\text{MgO}/\text{NCS-CC}$  has the better OER performance than that of  $\text{NCS-CC}$  (Fig. S9a, Supplementary data). Especially, the TOF value of  $\text{MgO}/\text{NCS-CC}$  is  $0.025\text{ s}^{-1}$  at the overpotential of 170 mV, which demonstrates the excellent intrinsic electrocatalytic activity of it (Fig. S9b, Supplementary data). In addition, as well known, the lower Tafel slope means the higher OER reaction rate and is more favorable for practical application. As shown in Fig. 4b, the curves of all samples are fitted to Tafel equation ( $\eta = a + b \log |j|$ ), where  $b$  is the Tafel slope. The Tafel slope of  $\text{MgO}/\text{NCS-CC}$  ( $114.7\text{ mV}\cdot\text{dec}^{-1}$ ) is much lower than that of  $\text{NCS-CC}$  ( $137.8\text{ mV}\cdot\text{dec}^{-1}$ ), which verifies the construction of heterostructure between  $\text{MgO}$  and  $\text{NiCo}_2\text{S}_4$  effectively improved the reaction rate and the kinetics of OER. Meanwhile, by extrapolating the Tafel plots to an overpotential of 0 mV, the exchange current density ( $j_0$ ) for the OER on  $\text{MgO}/\text{NCS-CC}$  and  $\text{NCS-CC}$  electrodes can be obtained, which represents the intrinsic activity of the electrocatalysts. As presented in Fig. S10 (Supplementary data),  $\text{MgO}/\text{NCS-CC}$  exhibits the higher  $j_0$  of  $0.2974\text{ mA}\cdot\text{cm}^{-2}$  than that of  $\text{NCS-CC}$  ( $0.2473\text{ mA}\cdot\text{cm}^{-2}$ ), which indicates more favorable proton discharge kinetics of  $\text{MgO}/\text{NCS-CC}$ . More importantly, compared with other samples reported in literature,  $\text{MgO}/\text{NCS-CC}$  exhibits the lowest OER overpotential at  $10\text{ mA}\cdot\text{cm}^{-2}$ , which indicates the activity of  $\text{MgO}/\text{NCS-CC}$  in pH-neutral condition is the best

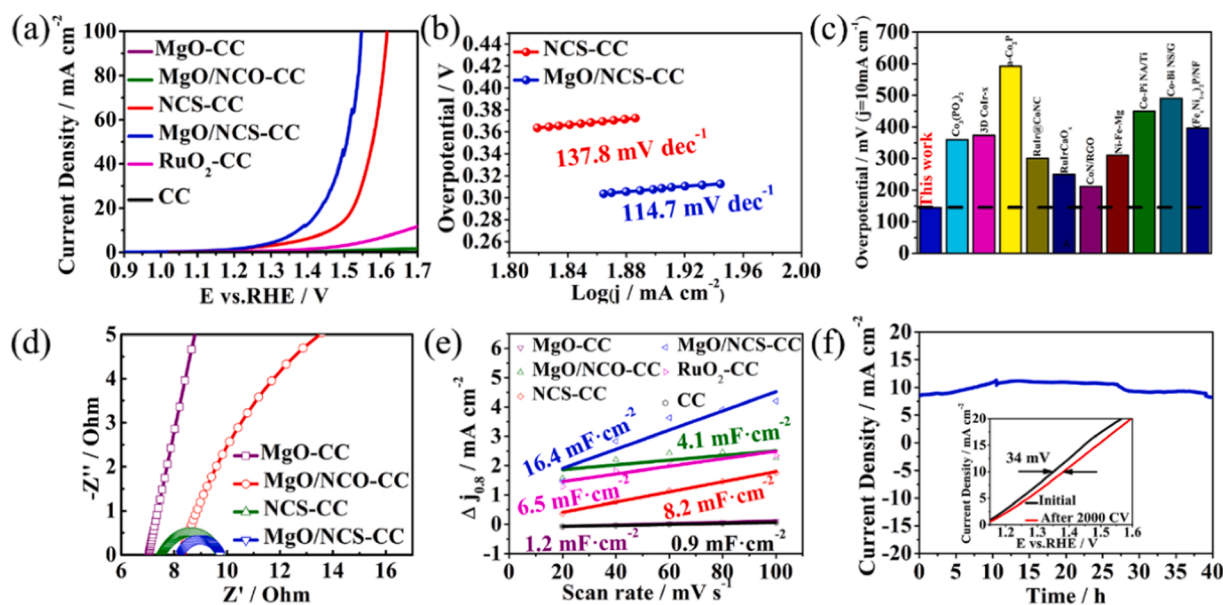


**Fig. 4.** (a) Polarization curves of OER in  $\text{CO}_2$ -saturated 0.5 M  $\text{KHCO}_3$  ( $\text{pH} \approx 8.5$ ) with 95% iR correction. (b) Tafel slopes of  $\text{MgO}/\text{NCS-CC}$  and  $\text{NCS-CC}$ . (c) The overpotential comparison between  $\text{MgO}/\text{NCS-CC}$  and other OER catalysts reported in literature in pH-neutral electrolyte at  $10\text{ mA}\cdot\text{cm}^{-2}$ . (d) Nyquist plots of fitted data for different electrodes at 200 mV. (e) The differences of current density at 0.773 V versus RHE plotted against the scan rate and fitted to a linear regression allows for the estimation of  $C_{dl}$ . (f) Long-term chronopotentiometric test of  $\text{MgO}/\text{NCS-CC}$ . (Inset image: polarization curves of OER before and after 2000 CV cycles).

in currently reported OER catalysts (Fig. 4c, Table S1, Supplementary data). As is well known that the effect of electrolyte on OER activity mainly depends on its pH value. It should be clarified that although the specific electrolyte in each electrocatalytic OER system shown in Fig. 4c is different, their pH values are close and are all pH-neutral mediums, which suggests that the OER performance of the catalysts is almost unaffected by the different electrolytes in the solutions.

To further study the electrocatalytic activity of MgO/NCS-CC, the electrochemical impedance spectroscopy (EIS) tests were applied from 100,000 to 0.04 Hz. The fitted data of the Nyquist plots by the one-time model (Fig. S11, Supplementary data) for MgO/NCS-CC and other samples at the overpotential of 200 mV are given in Fig. 4d, and the values of corresponding charge transfer resistance ( $R_{ct}$ ) are also given in Table S2 (Supplementary data). Compared with other reference samples, the  $R_{ct}$  of MgO/NCS-CC is 1.47  $\Omega$ , which is the lowest among the four samples. Notably, MgO/NCS-CC exhibits the fastest charge-transport kinetics during the OER process compared with that of MgO-CC, MgO/NCO-CC and NCS-CC, which is beneficial for the OER activity. It is noted that the different initial points of EIS plots may be due to the different amount of electrolyte used for each test, which represents the solution resistance and this phenomena is common in other reported works especially in pH-neutral medium. The values of  $R_s$  have also been given in Table S2 (Supplementary data). Additionally, the electrochemical active surface area (ECSA) was performed to analyze the intrinsic activity of catalysts, and it was estimated by the value of double-layer capacitances ( $C_{dl}$ ). Moreover, the  $C_{dl}$  was measured by the cyclic voltammetry (CV) at the scan rate from 20  $\text{mV}\cdot\text{s}^{-1}$  to 100  $\text{mV}\cdot\text{s}^{-1}$  (Fig. S12, Supplementary data). As expected, the ECSA of MgO/NCS-CC is 16.4  $\text{mF}\cdot\text{cm}^{-2}$ , which the value is larger than that of NCS-CC (8.2  $\text{mF}\cdot\text{cm}^{-2}$ ), NFO-CC (4.1  $\text{mF}\cdot\text{cm}^{-2}$ ), RuO<sub>2</sub> (6.5  $\text{mF}\cdot\text{cm}^{-2}$ ), MgO-CC (1.2  $\text{mF}\cdot\text{cm}^{-2}$ ) and CC (0.9  $\text{mF}\cdot\text{cm}^{-2}$ ), suggesting MgO/NCS-CC possess more accessible active sites than other reference samples (Fig. 4e). Notably, the more active sites are favorable for the better OER performance, which also confirms the effectiveness of constructing heterostructure between MgO and NiCo<sub>2</sub>S<sub>4</sub> to promote the OER catalytic performance. Additionally, the LSV curves were also normalized to the value of ECSA to explore the intrinsic activity of catalysts. As indicated in Fig. S13 (Supplementary data), the current density of MgO/NCS-CC after the normalization remains much higher than that of other control catalysts, which means the best intrinsic activity of MgO/NCS-CC for OER in pH-neutral electrolyte.

To analyze the stability of MgO/NCS-CC in neutral electrolyte, the long-term chronopotentiometry *i*-*t* test at the current density of 10  $\text{mA}\cdot\text{cm}^{-2}$  was performed. The current density almost unchanged during 40 h *i*-*t* test, which demonstrates the excellent electrochemical stability of MgO/NCS-CC during the OER process in neutral electrolyte (Fig. 4f). The inset image in Fig. 4f shows the LSV cycles of MgO/NCS-CC before and after 2000 CV cycles in the potential range of OER, from which it can be seen that the overpotential increased only 34 mV after the long-term CV test, suggesting the excellent stability of MgO/NCS-CC in neutral water oxidation.

### 3.3. Morphology, structure and surface chemical composition after long-term test

The transition metal catalysts for OER usually induce different degrees of surface reconstruction. Therefore, it is necessary to characterize the structure, morphology and electronic structure of MgO/NCS-CC after long-term OER test, and further ensure the stability of the catalyst. Herein, XRD was firstly performed to explore the crystal structure of MgO/NCS-CC before and after long-term test. The XRD pattern of MgO/NCS-CC after 2000 CV cycles still shows the main peaks at 31.6°, 38.3°, 50.5°, and 55.3°, which can be ascribed to NiCo<sub>2</sub>S<sub>4</sub> (JCPDF No.20–0781) and the peak at 42.9° can be attributed to MgO (JCPDF No.45–0946). Furthermore, compared with the XRD pattern of MgO/NCS-CC before the cycle test, the XRD peaks of MgO/NCS-CC after long-term test only

show slight peak shifts, which indicates the main structure is still maintained. Meanwhile, the decrease of intensity of XRD peaks also suggests the shedding and loss of the catalyst during the process of the long-term OER test, which is a normal phenomenon. The peak at 25.5° indicates the exposure of CC after the long-term OER test (Fig. S14, Supplementary data). Moreover, the SEM images of MgO/NCS-CC after 2000 CV cycles reveal that the morphology of MgO/NCS-CC only has slight change compared with the initial morphology (Fig. S15a, Fig. S15c, Supplementary data), which indicates the excellent stability of MgO/NCS-CC. However, in a larger scale, compared with the morphology of the initial sample, the catalyst had some shedding from CC during the long-term OER test (Fig. S15b, Fig. S15d, Supplementary data), which the phenomena verified the XRD analysis. Furthermore, the XPS comparison of MgO/NCS-CC before and after long-term OER tests was also used to analyze the change of electronic structure of the catalyst (Fig. S16, Supplementary data). The XPS survey spectrum demonstrates that all elements can be found in the sample of MgO/NCS-CC after long-term OER test (Fig. S16a, Supplementary data). More importantly, the high-resolution XPS spectra comparison of MgO/NCS-CC before and after long-term OER tests shows negligible peak shifts of Ni 2p<sub>3/2</sub>, Co 2p<sub>3/2</sub> and Mg 1s, which manifests the excellent stability of the electronic structure of MgO/NCS-CC (Fig. S16b–d, Supplementary data). Moreover, the high-resolution XPS spectra of O 1s and S 2p of MgO/NCS-CC after long-term OER test also maintain negligible change compared with the initial MgO/NCS-CC, suggesting the stability of electronic structure of anions (Fig. S16e–f, Supplementary data). In addition, whether the lattice oxygen participates in the oxygen exchange can also be confirmed by XPS results. As shown in Fig. S16e, in the O 1s XPS spectra, the peak position, peak intensity and the peak area of M-O bond of the catalyst have almost no change before and after 2000 CV cycles, which suggests that the lattice oxygen doesn't participate in the oxygen exchange [39]. The results of XRD, SEM and XPS of MgO/NCS-CC after long-term OER test confirm the excellent stability and durability of MgO/NCS-CC from the respective aspects of crystal structure, morphology, and electronic structure, which the results are also consistent with the results from the long-term OER test.

### 3.4. Theoretical considerations

To rationalize the improved OER performance of the MgO (111)/NiCo<sub>2</sub>S<sub>4</sub> (111), we have carried out the DFT calculations using the three structures shown in the Fig. 5a–c. The computational details are described in the Supporting Information. As shown in Fig. S17 (Supplementary data), the projected density of states (PDOS) of MgO (111), NiCo<sub>2</sub>S<sub>4</sub> (111) and MgO (111)/NiCo<sub>2</sub>S<sub>4</sub> (111) demonstrate that MgO (111) has semiconductor-like electronic structure, while NiCo<sub>2</sub>S<sub>4</sub> (111) and MgO (111)/NiCo<sub>2</sub>S<sub>4</sub> (111) have metallic like electronic structures, and the integral area of the density of states near Fermi level ( $E_F$ ) for MgO (111)/NiCo<sub>2</sub>S<sub>4</sub> (111) system is larger than that of other systems (Fig. 5d) [40–42]. Thus, the intensity of electrical conductivity decreases in the following order: MgO (111)/NiCo<sub>2</sub>S<sub>4</sub> (111) > NiCo<sub>2</sub>S<sub>4</sub> (111) > MgO (111), leading to the catalytic activity of three catalysts on the same trend. As shown in Fig. 5e, the calculated adsorption energies show that MgO (111) has much lower H<sub>2</sub>O adsorption energy (−0.90 eV) than NiCo<sub>2</sub>S<sub>4</sub> (111) (−0.53 eV), indicating that MgO is a better adsorption water material. After introducing MgO into NiCo<sub>2</sub>S<sub>4</sub> and forming the heterostructure, the H<sub>2</sub>O adsorption energy of NiCo<sub>2</sub>S<sub>4</sub> (111) decreases to −0.83 eV, resulting in the enhanced H<sub>2</sub>O adsorption compared to NiCo<sub>2</sub>S<sub>4</sub> (111), which increases the H<sub>2</sub>O dissociation for the generation of hydrogen and oxygen [43,44].

In order to further identify a rate-determining step, we have calculated thermodynamic free energy diagrams for the OER in the MgO (111), NiCo<sub>2</sub>S<sub>4</sub> (111) and MgO (111)/NiCo<sub>2</sub>S<sub>4</sub> (111) surfaces as a function of electrode potential (*U*). The side view structures of \*OH, \*O and \*OOH absorbed on MgO (111), NiCo<sub>2</sub>S<sub>4</sub> (111) and MgO (111)/NiCo<sub>2</sub>S<sub>4</sub> (111) are shown in Fig. S18 (Supplementary data). The results

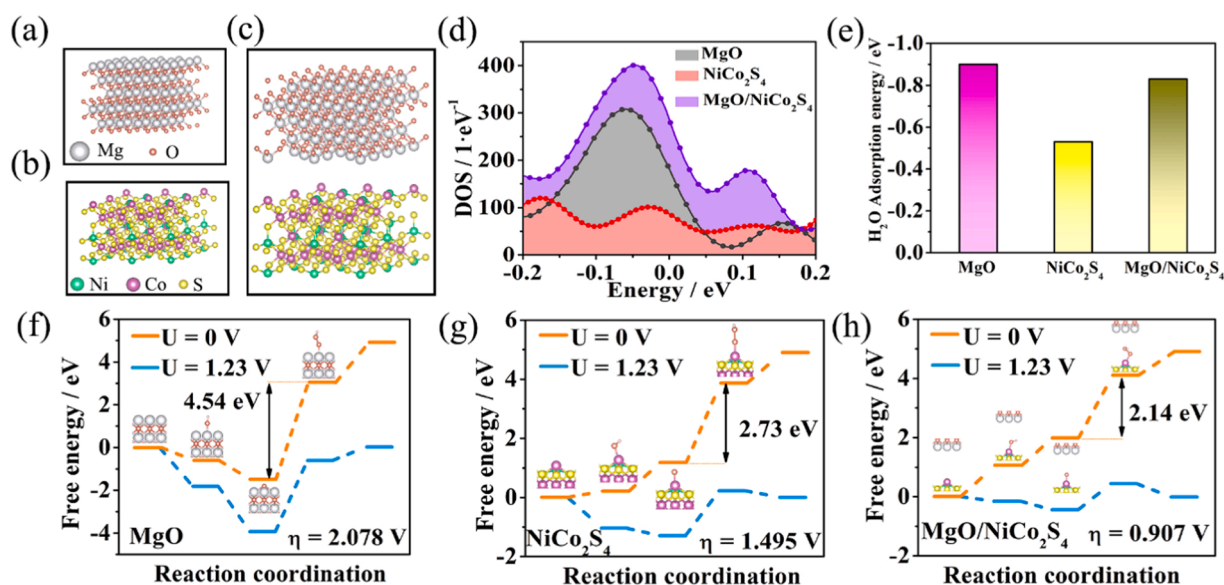


**Fig. 5.** (a-c) Geometries of MgO (111), NiCo<sub>2</sub>S<sub>4</sub> (111) and MgO (111)/NiCo<sub>2</sub>S<sub>4</sub> (111). (d) Density of states (DOS) of MgO (111), NiCo<sub>2</sub>S<sub>4</sub> (111) and MgO (111)/NiCo<sub>2</sub>S<sub>4</sub> (111). (e) Adsorption energies of H<sub>2</sub>O on MgO (111), NiCo<sub>2</sub>S<sub>4</sub> (111) and MgO (111)/NiCo<sub>2</sub>S<sub>4</sub> (111). (f-h) Free energies of OER reaction steps for MgO (111), NiCo<sub>2</sub>S<sub>4</sub> (111) and MgO (111)/NiCo<sub>2</sub>S<sub>4</sub> (111) systems. Insets show the partial optimized configurations with different substrates. Golden and white balls denote the O and H atoms.

indicate that the overpotentials for OER are governed by the same rate-determining steps associated with the \*OOH formation (Fig. 5f-h) [45], while the corresponding energy barriers are much different. The elementary reaction and the corresponding reaction barrier for each step of pH-neutral OER for MgO/NCS-CC, NCS-CC, and MgO-CC are respectively shown in Table S3 in the Supplementary data. The higher energy barrier, the larger overpotentials (η) for OER. The energy barrier of \*OOH formation in MgO (111) is the highest (4.54 eV), which reduces to 2.73 eV in NiCo<sub>2</sub>S<sub>4</sub> (111) and 2.14 eV in MgO (111)/NiCo<sub>2</sub>S<sub>4</sub> (111), leading to the η of three surfaces decreases in the order: MgO (111) (2.078 V) > NiCo<sub>2</sub>S<sub>4</sub> (111) (1.495 V) > MgO (111)/NiCo<sub>2</sub>S<sub>4</sub> (111) (0.907 V). The notable 0.588 V drop in η provides a valid evidence that the OER performance is enhanced in the MgO (111)/NiCo<sub>2</sub>S<sub>4</sub> (111) once the MgO is introduced, agreeing well with experimental data.

The excellent OER activity of MgO/NCS-CC in pH-neutral electrolyte can be attributed to the following reasons: a) The introduction of HEP element Mg in the heterostructure can significantly improve the adsorption of H<sub>2</sub>O on the surface of catalyst. b) The construction of heterostructure between MgO and NiCo<sub>2</sub>S<sub>4</sub> can successfully regulate the electronic state of Ni, Co and Mg to the states which are beneficial for improving the catalytic activity. c) The larger ECAS area and lower R<sub>ct</sub> of MgO/NCS-CC are also advantageous for the OER performance. d) The method of in-situ growth of the catalyst on carbon cloth can provide a 3D self-supported electrode for MgO/NCS, which is advantageous to the electrocatalyst/electrolyte contact and can accelerate the charge transfer.

#### 4. Conclusion

In summary, the heterostructure MgO/NCS-CC between MgO and NiCo<sub>2</sub>S<sub>4</sub> was successfully constructed on carbon cloth by multiple steps. The MgO/NCS-CC exhibits outstanding OER activity especially in pH-neutral electrolyte with the overpotential of 145 mV and Tafel slope of 114.7 mV·dec<sup>-1</sup> at the current density of 10 mA·cm<sup>-2</sup>, which is among the best of various neutral OER catalysts reported. Moreover, MgO/NCS-CC also reveals the excellent stability. Based on the experimental and DFT analysis, the outstanding OER performance can be ascribed to: a) The strong adsorption of water molecules induced by the introduction of HEP element Mg. b) The optimized electronic structure

for OER in pH-neutral electrolyte, which is regulated by the construction of the heterostructure. c) Favorable charge transfer and electrocatalyst/electrolyte contact which are benefited from the in-situ growth on self-supporting carbon cloth. Undoubtedly, this study not only provides a new strategy to construct heterostructure and enhance water adsorption on the surface of catalyst, but also, provides a new method to fabricate non-noble metal-based catalysts for OER in pH-neutral condition.

#### CRediT authorship contribution statement

**Wei-Zhe Chen:** Software, Data curation, Investigation, Writing – original draft. **Meng Zhang:** Investigation, Software. **Yang Liu:** Software, Data curation. **Xiao-Man Yao:** Investigation. **Peng-Yu Liu:** Software. **Zhiliang Liu:** Writing – review & editing. **Jinlu He:** Investigation, Writing – original draft, DFT calculations. **Yan-Qin Wang:** Supervision, Conceptualization, Writing – review & editing, Project administration.

#### Declaration of Competing Interest

The authors declare no competing financial interests.

#### Acknowledgements

We are thankful for the financial support from NSFC (Grants 22162020, 21761022), the Inner Mongolia Autonomous Region Natural Science Fund Project (2021MS02016, 2017MS0204).

#### Appendix A. Supporting information

Supplementary data associated with this article can be found in the online version at doi:10.1016/j.apcatb.2022.121432.

#### References

- [1] J.X. Feng, H. Xu, Y.T. Dong, S.H. Ye, Y.X. Tong, G.R. Li, FeOOH/Co/FeOOH hybrid nanotube arrays as high-performance electrocatalysts for the oxygen Evolution Reaction, *Angew. Chem. Int. Ed.* 55 (2016) 3694–3698.
- [2] Y. Shao, X. Xiao, Y.P. Zhu, T.Y. Ma, Single-crystal cobalt phosphate nanosheets for biomimetic oxygen evolution in neutral electrolytes, *Angew. Chem. Int. Ed.* 58 (2019) 14599–14604, 21.

- [3] Y. Zhang, C. Wu, H. Jiang, Y. Lin, H. Liu, Q. He, S. Chen, T. Duan, L. Song, Atomic iridium incorporated in cobalt hydroxide for efficient oxygen evolution catalysis in neutral electrolyte, *Adv. Mater.* 30 (2018), 1707522.
- [4] K. Xu, H. Cheng, L. Liu, H. Lv, X. Wu, C. Wu, Y. Xie, Promoting active species generation by electrochemical activation in alkaline media for efficient electrocatalytic oxygen evolution in neutral media, *Nano Lett.* 17 (2017) 578–583.
- [5] K.F. Lu, G.R. Chang, H. Zhang, X.Y. Yu, Accelerating the oxygen evolution reaction kinetics of  $\text{Co}_3\text{O}_4$  in neutral electrolyte by decorating  $\text{RuO}_2$ , *Chem. Commun.* 57 (2021) 2907.
- [6] C. Liu, B.C. Colon, M. Ziesack, P.A. Silver, D.G. Nocera, Water splitting–biosynthetic system with  $\text{CO}_2$  reduction efficiencies exceeding photosynthesis, *Science* 352 (2016) 1210.
- [7] X. Zheng, B. Zhang, P. De Luna, Y. Liang, R. Comin, O. Voznyy, L. Han, F.P. Garcia de Arquer, M. Liu, C.T. Dinh, T. Regier, J.J. Dynes, S. He, H.L. Xin, H. Peng, D. Prendergast, X. Du, E.H. Sargent, Theory-driven design of high-valence metal sites for water oxidation confirmed using in situ soft X-ray absorption, *Nat. Chem.* 10 (2018) 149–154.
- [8] J. Xu, J. Li, Z. Lian, A. Araujo, Y. Li, B. Wei, Z. Yu, O. Bondarchuk, I. Amorim, V. Tileli, B. Li, L. Liu, Atomic-step enriched ruthenium–iridium nanocrystals anchored homogeneously on MOF-derived support for efficient and stable oxygen evolution in acidic and neutral media, *ACS Catal.* 11 (2021) 3402–3413.
- [9] Y. Kim, W.J. Woo, D. Kim, S. Lee, S.M. Chung, J. Park, H. Kim, Atomic-layer-deposition-based 2D transition metal chalcogenides: synthesis, modulation, and applications, *Adv. Mater.* (2021), 2005907.
- [10] F. Yang, T. Xiong, P. Huang, S. Zhou, Q. Tan, H. Yang, Y. Huang, M.S. Balogun, Nanostructured transition metal compounds coated 3D porous core-shell carbon fiber as monolith water splitting electrocatalysts: a general strategy, *Chem. Eng. J.* 423 (2021), 130279.
- [11] J. Sun, H. Xue, N. Guo, T. Song, Y.R. Hao, J. Sun, J. Zhang, Q. Wang, Synergetic metal defect and surface chemical reconstruction into  $\text{NiCo}_2\text{S}_4/\text{ZnS}$  heterojunction to achieve outstanding electrocatalysis performance, *Angew. Chem. Int. Ed.* 60 (2021) 19435–19441.
- [12] Q. Liang, G. Brocks, A. Bieberle-Hütter, Oxygen evolution reaction (OER) mechanism under alkaline and acidic conditions, *J. Phys. Energy* 3 (2021), 026001.
- [13] M. Bajdich, M. Garcia-Mota, A. Vojvodic, J.K. Nørskov, A.T. Bell, Theoretical investigation of the activity of cobalt oxides for the electrochemical oxidation of water, *J. Am. Chem. Soc.* 135 (2013) 13521–13530.
- [14] L. Zhang, L. Wang, Y. Wen, F. Ni, B. Zhang, H. Peng, Boosting neutral water oxidation through surface oxygen modulation, *Adv. Mater.* 32 (2020), 2002297.
- [15] D. Guo, Z. Zeng, Z. Wan, Y. Li, B. Xi, C. Wang, A CoN-based OER electrocatalyst capable in neutral medium: atomic layer deposition as rational strategy for fabrication, *Adv. Funct. Mater.* 31 (2021), 2101324.
- [16] N. Wang, Z. Cao, X. Zheng, B. Zhang, S.M. Kozlov, P. Chen, C. Zou, X. Kong, Y. Wen, M. Liu, Y. Zhou, C.T. Dinh, L. Zheng, H. Peng, Y. Zhao, L. Cavallo, X. Zhang, E.H. Sargent, Hydration-effect-promoting Ni-Fe oxyhydroxide catalysts for neutral water oxidation, *Adv. Mater.* 32 (2020), 1906806.
- [17] G. Zhao, K. Rui, S.X. Dou, W. Sun, Heterostructures for electrochemical hydrogen evolution reaction: a review, *Adv. Funct. Mater.* 28 (2018), 1803291.
- [18] Q. Zhang, F. Luo, X. Long, X. Yu, K. Qu, Z. Yang, N. P. doped carbon nanotubes confined WN-Ni Mott-Schottky heterogeneous electrocatalyst for water splitting and rechargeable zinc-air batteries, *Appl. Catal. B* 298 (2021), 120511.
- [19] H. Li, S. Chen, Y. Zhang, Q. Zhang, X. Jia, Q. Zhang, L. Gu, X. Sun, L. Song, X. Wang, Systematic design of superaerophobic nanotube-array electrode comprised of transition-metal sulfides for overall water splitting, *Nat. Commun.* 9 (2018) 2452.
- [20] Z. Lu, W. Zhu, X. Yu, H. Zhang, Y. Li, X. Sun, X. Wang, H. Wang, J. Wang, J. Luo, X. Lei, L. Jiang, Ultrahigh hydrogen evolution performance of under-water “Superaerophobic”  $\text{MoS}_2$  nanostructured electrodes, *Adv. Mater.* 26 (2014) 2683–2687.
- [21] B. Cao, Y. Cheng, M. Hu, P. Jing, Z. Ma, B. Liu, R. Gao, J. Zhang, Efficient and durable 3D self-supported nitrogen-doped carbon-coupled Nickel/Cobalt phosphide electrodes: stoichiometric ratio regulated phase- and morphology-dependent overall water splitting performance, *Adv. Funct. Mater.* 29 (2019), 1906316.
- [22] H. Sun, Z. Yan, F. Liu, W. Xu, F. Cheng, J. Chen, Self-supported transition-metal-based electrocatalysts for hydrogen and oxygen evolution, *Adv. Mater.* 32 (2020), 1806326.
- [23] X. Gao, X. Li, Y. Yu, Z. Kou, P. Wang, X. Liu, J. Zhang, J. He, S. Mu, J. Wang, Synergizing aliovalent doping and interface in heterostructured NiV nitride@oxyhydroxide core-shell nanosheet arrays enables efficient oxygen evolution, *Nano Energy* 85 (2021), 105961.
- [24] Y. Liu, J. Zhang, S. Wang, S. Jiang, Q. Liu, X. Li, Z. Wu, G. Yu, Ru catalyst-induced perpendicular magnetic anisotropy in  $\text{MgO}/\text{CoFeB}/\text{Ta}/\text{MgO}$  multilayered films, *ACS Appl. Mater. Interfaces* 7 (2015) 26643–26648.
- [25] X.D. Lou, Phosphorized  $\text{CoNi}_2\text{S}_4$  yolk-shell spheres for highly efficient hydrogen production via water and urea electrolysis, *Angew. Chem. Int. Ed.* 60 (2021) 22885–22891.
- [26] H. Xu, C. Shan, X. Wu, M. Sun, B. Huang, Y. Tang, C.-H. Yan, Fabrication of layered double hydroxide microcapsules mediated by cerium doping in metal–organic frameworks for boosting water splitting, *Energy Environ. Sci.* 13 (2020) 2949–2956.
- [27] L. Zeng, K. Sun, X. Wang, Y. Liu, Y. Pan, Z. Liu, D. Cao, Y. Song, S. Liu, C. Liu, Three-dimensional-networked  $\text{Ni}_2\text{P}/\text{Ni}_3\text{S}_2$  heteronanoflake arrays for highly enhanced electrochemical overall-water-splitting activity, *Nano Energy* 51 (2018) 26–36.
- [28] M. Han, N. Wang, B. Zhang, Y.J. Xia, J. Li, J.R. Han, K.L. Yao, C.C. Gao, C.N. He, Y. C. Liu, Z.M. Wang, A. Seifitokaldani, X.H. Sun, H.Y. Liang, High-valent nickel promoted by atomically embedded copper for efficient water oxidation, *ACS Catal.* 10 (2020) 9725–9734.
- [29] J.S. Li, J.J. Ma, K. Du, E.L. Zhao, J.X. Guo, J. Mao, T. Ling, Double exchange interaction promoted high-valence metal sites for neutral oxygen evolution reaction, *Chem. Commun.* 56 (2020) 15004.
- [30] X. Hao, Z. Jiang, B. Zhang, X. Tian, C. Song, L. Wang, T. Maiyalagan, X. Hao, Z. J. Jiang, N-doped carbon nanotubes derived from graphene oxide with embedment of FeCo nanoparticles as bifunctional air electrode for rechargeable liquid and flexible all-solid-state zinc–air batteries, *Adv. Sci.* 8 (2021), 2004572.
- [31] T. Wang, P. Wang, W. Zang, X. Li, D. Chen, Z. Kou, S. Mu, J. Wang, Nanoframes of  $\text{Co}_3\text{O}_4\text{--Mo}_2\text{N}$  heterointerfaces enable high-performance bifunctionality toward both electrocatalytic HER and OER, *Adv. Funct. Mater.* (2021), 2107382.
- [32] Y. Zhang, J. Xie, Y. Han, C. Li, Dual-salt Mg-based batteries with conversion cathodes, *Adv. Funct. Mater.* 25 (2015) 7300–7308.
- [33] S. Chen, S. Liang, B. Wu, Z. Lan, Z. Guo, H. Kobayashi, X. Yan, R. Li, Existence of solid electrolyte interphase in Mg batteries: Mg/S chemistry as an example, *ACS Appl. Mater. Interfaces* 11 (2019) 33946–33954.
- [34] T. Gao, S. Hou, K. Huynh, F. Wang, N. Eidson, X. Fan, F. Han, C. Luo, M. Mao, X. Li, C. Wang, Ultrasmall silver clusters stabilized on MgO for robust oxygen-promoted hydrogen production from formaldehyde reforming, *ACS Appl. Mater. Interfaces* 10 (2018) 14767–14776.
- [35] X. Luo, P. Ji, P. Wang, R. Cheng, D. Chen, C. Lin, J. Zhang, J. He, Z. Shi, N. Li, S. Xiao, S. Mu, Interface engineering of hierarchical branched Mo-doped  $\text{Ni}_3\text{S}_2/\text{Ni}_x\text{Py}$  hollow heterostructure nanorods for efficient overall water splitting, *Adv. Energy Mater.* 10 (2020), 1903891.
- [36] L. An, B. Huang, Y. Zhang, R. Wang, N. Zhang, T. Dai, P. Xi, C.H. Yan, Interfacial defect engineering for improved portable zinc–air batteries with a broad working temperature, *Angew. Chem. Int. Ed.* 58 (2019) 9459–9463.
- [37] S. Wang, Y. Cao, W. Jia, Z. Lu, D. Jia, A cage-confinement strategy to fabricate  $\text{Pt-Mo}_6\text{Co}_6\text{C}$  heterojunction for highly efficient PH-universal hydrogen evolution, *Appl. Catal. B* 298 (2021), 120579.
- [38] J. Sun, T. Song, Z. Shao, N. Guo, K. Huang, F. He, Q. Wang, Interfacial electronic structure modulation of hierarchical  $\text{Co(OH)F}/\text{CuCo}_2\text{S}_4$  nanocatalyst for enhanced electrocatalysis and Zn–air batteries performances, *ACS Appl. Mater. Interfaces* 11 (2019) 37531–37540.
- [39] Y.R. Xue, J.J. Fang, X.D. Wang, Z.Y. Xu, Y.F. Zhang, Q.Q. Lv, M.Y. Liu, W. Zhu, Z. B. Zhuang, Sulfate-functionalized  $\text{RuFeO}_x$  as highly efficient oxygen evolution reaction electrocatalyst in acid, *Adv. Funct. Mater.* 31 (2021), 2101405.
- [40] P. Zhang, Y. Liu, T. Liang, E.H. Ang, X. Zhang, F. Ma, Z. Dai, Nitrogen-doped carbon wrapped  $\text{Co-Mo}_2\text{C}$  dual Mott–Schottky nanosheets with large porosity for efficient water electrolysis, *Appl. Catal. B* 284 (2021), 119738.
- [41] W.-Z. Chen, P.-Y. Liu, L. Zhang, Y. Liu, Z. Liu, J. He, Y.-Q. Wang, High-efficient and durable overall water splitting performance by interfacial engineering of Fe-doped urchin-like  $\text{Ni}_2\text{P}/\text{Ni}_3\text{S}_2$  heterostructure, *Chem. Eng. J.* 424 (2021), 130434.
- [42] P.-Y. Liu, K. Shi, W.-Z. Chen, R. Gao, Z.-L. Liu, H. Hao, Y.-Q. Wang, Enhanced electrocatalytic nitrogen reduction reaction performance by interfacial engineering of MOF-based sulfides  $\text{FeNi}_2\text{S}_4/\text{NiS}$  hetero-interface, *Appl. Catal. B* 287 (2021), 119956.
- [43] B. Geng, F. Yan, X. Zhang, Y. He, C. Zhu, S.L. Chou, X. Zhang, Y. Chen, Conductive CuCo-based bimetal framework for efficient hydrogen evolution, *Adv. Mater.* (2021), 21067812.
- [44] L. Deng, F. Hu, M. Ma, S.C. Huang, Y. Xiong, H.Y. Chen, L. Li, S. Peng, Electronic modulation caused by interfacial Ni–O–M (M = Ru, Ir, Pd) bonding for accelerating hydrogen evolution kinetics, *Angew. Chem. Int. Ed.* 60 (2021) 22276–22282.
- [45] M. Han, C. Wang, J. Zhong, J. Han, N. Wang, A. Seifitokaldani, Y. Yu, Y. Liu, X. Sun, A. Vomiero, H. Liang, Promoted self-construction of  $\beta\text{-NiOOH}$  in amorphous high entropy electrocatalysts for the oxygen evolution reaction, *Appl. Catal. B* 301 (2022), 120764.